Tomaž Rus
Turboinštitut d.d.,
Rovšnikova 7,
1210 Ljubljana-Šentvid, Slovenia
e-mail: tomaz.rus@turboinstitut.si

Matevž Dular[1]
e-mail: matevz.dular@fs.uni-lj.si

Brane Širok
e-mail: brane.sirok@fs.uni-lj.si

Marko Hočevar
e-mail: marko.hocevar@fs.uni-lj.si

Laboratory for Water and Turbine Machines,
University of Ljubljana,
Aškerčeva 6,
1000 Ljubljana, Slovenia

Igor Kern
Turboinštitut d.d., Rovšnikova 7, 1210
Ljubljana-Šentvid, Slovenia
e-mail: igor.kern@turboinstitut.si

An Investigation of the Relationship Between Acoustic Emission, Vibration, Noise, and Cavitation Structures on a Kaplan Turbine

The goal of the study was to explain the relationship between different acoustic signals and visual appearance of cavitation. Measurements of acoustic emission, vibration, and noise were performed on a Kaplan turbine model, with only two blades, in a cavitating condition. Since a model with only two blades was used, most of the side effects were eliminated, and it was concluded that the cavitation itself is the source of the recorded signal. Results showed an interesting relationship between the extent of the cavitation and the recorded data from sensors. At a decreasing cavitation number, the recorded amplitudes from all measurements first rose, experienced a local maximum, then fell to a local minimum, and finally rose again. The cavitation was also visually observed. It was concluded from the measurements that there are distinct correlations between acoustic emission, vibration, and noise on one side and the topology, extent, and type of cavitation structures on the other side. A physical explanation for the phenomenon was introduced and included in a semi-empirical model that links the visual appearance of cavitation on the blade of the turbine to the generated noise and vibration. [DOI: 10.1115/1.2754313]

1 Introduction

The phenomenon of cavitation, characterized by vapor generation and condensation, occurs frequently in hydraulic machines. It causes vibration, increase of hydrodynamic drag, changes in the flow hydrodynamics, erosion, thermal and light effects (such as luminescence), generation of noise, and acoustic emission.

The most commonly used method for identifying the presence of cavitation in hydraulic machines is based on observations of the drop in efficiency. It must be noted that cavitation starts to develop before the usual "critical" point, the 1% drop in efficiency in turbine model testing. It is generally accepted that the pressure for inception of cavitation is not constant and varies with fluid physical properties and the surface roughness of the hydraulic equipment. Other techniques, such as vibration analysis [1–3], hydrophone observations, and application of the high-frequency acoustic emission technique [4–6] in condition monitoring of rotating machinery, have been growing over recent years. Typical frequencies associated with these techniques range from 5 kHz to 1 MHz. On the other hand, in model testing, visualization of cavitation is becoming an important aspect of cavitation research [7–9]. The interesting trend, where when the cavitation number is decreased, the measured signal first rises, experiences a local maximum, then falls to the local minimum, and rises again, is actually well known and was first reported by Pearsall [10] who investigated cavitation noise and vibration in a centrifugal pump. A similar trend on an inducer pump was also measured by Gopalakrishan [11]. However, a thorough explanation of the trend was never given.

This paper discusses the measurements of acoustic emission, vibration, and noise on a two-bladed Kaplan turbine. Parallel to conventional measurements, images of cavitation structures were recorded. It was discovered that a correlation exists between the acoustic emission, vibration, and noise on one side, and topology, type, and extent of cavitation structures on the other side. Finding deterministic links between the acoustical signal and the cavitation structures could lead to improvement of the monitoring and control of hydraulic machines.

A physical explanation of the processes involved in the noise generation is given in this paper. To quantify our observations, the conclusions drawn from the results of experiment are introduced as a semi-empirical model that also includes theories of cavitation cloud collapse [12,13] and attenuation of the pressure wave [14]. A similar model was previously successfully used for the prediction of cavitation erosion on different geometries [15,16]. The present model could be used to predict the cavitation noise and also to determine the type of cavitation that appears in turbines.

2 Experimental Setup

Experiments were performed at the low head closed-loop test rig for Kaplan turbines (Fig. 1). Model tests were performed according to IEC 60193 standard [17]. The flow rate was measured with an absolute accuracy of ±0.16% of the measured value (Venturimeter calibrated with volumetric method) and ±0.20% of the measured value (electromagnetic flowmeter). The head was measured with an uncertainty of less than ±0.1% of the measured value.

Experiments were first conducted on a four-bladed Kaplan turbine model with specific speed $n_q = 3.21$ and nominal outside diameter of 350 mm. The Reynolds number was held constant during the experiment $Re = 2.6 \times 10^6$ (based on the blade tip velocity and the blade chord length).

Because of the distorted signals from noise, the measured acoustic signals from the four-bladed turbine show an unclear cavitation trend from the interaction of multiple blades. This unclear trend is also demonstrated from the visual measurements. In order to isolate the cavitation features, a two-bladed Kaplan tur-

Copyright © 2007 by ASME
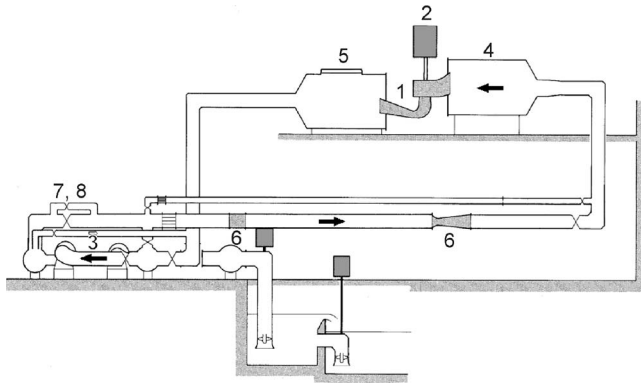
Fig. 1 Low head closed-loop test rig for Kaplan turbine testing: 1, model turbine; 2, motor-generator; 3, circuit pumps; 4, pressure tank; 5, suction tank; 6, flowmeters; and 7 and 8, regulation and by-pass valves, respectively

bine was therefore constructed from the original four-blade configuration by removing two blades. The two-bladed turbine has, of course, higher specific speed than the original. The efficiency of the two-bladed turbine certainly deviates from the original design. However, a similar cavitation condition and phenomena would be expected with the same revolution speed, guide vane opening, flow rate, cavitation number, and lower head as for the original four-bladed turbine.

Because of the physical nature of cavitation, sensors with a large frequency range were used. The acoustic emission sensor and accelerometer were mounted on the flange in the horizontal plane at the beginning of the suction tube. The hydrophone was mounted on the suction tube close to the impeller. Actual positions of the sensors, stroboscopic light, and the charge-coupled device (CCD) camera can be seen in Fig. 2.

2.1 Acoustic Emission Sensor. For the detection of the high-frequency noise, an acoustic emission sensor Kistler 8152A1 was used. It contains a piezoelectric element that detects acoustical waves in solids with a frequency ranging from 50 kHz to 400 kHz ($\pm$10 dB). The sensor was mounted according to ASTM E 650-85 standard [18]. It was connected to the signal-conditioning device, a Kistler AE-Piezotron Coupler 5125A, which contains the sensor's current supply, the amplifier, a two-pole Butterworth highpass (50 kHz cutoff frequency), and low-pass (1 MHz cutoff frequency) filters.

2.2 Hydrophone. A Bruel and Kjær (B & K) type 8103 high-frequency hydrophone was used. It can be used for sound measurements with a frequency ranging from 0.1 Hz to 180 kHz. ($\pm$12.5 dB). The hydrophone was connected to the charge amplifier B&K-type 2635. The hydrophone was submerged in a small container filled with water and attached to the outside surface of the draft tube. The acoustical signal was transmitted from the flow field, through the Plexiglas and water to the hydrophone. To improve the amplitude resolution of the high-frequency component before A/D conversion, the low-frequency signal (up to 2 kHz) was removed with an analog filter KEMO VBF42.

2.3 Accelerometer. A Bruel and Kjær type 4393 accelerometer was used. It has a flat frequency response from 0.1 Hz to ~15 kHz. The typical mounted resonance frequency is ~55 kHz. The calibration curve was considered so that the vibrations could be measured almost up to the accelerometer resonance region (frequency range 30–50 kHz ($\pm$7 dB)). Despite this deficiency, the results were similar to those of the acoustic emission and hydrophone measurements. The accelerometer was connected to the amplifier B&K-type 2635.

2.4 Data Acquisition. The acoustic emission, hydrophone, accelerometer, and trigger signals were simultaneously sampled at a 12-bit resolution with a 1 MHz sampling rate for 20 s to preserve the full frequency range of each transducer for further analysis. To avoid the possible aliasing phenomenon, the sampling frequency was at least five times higher than the observed frequency range. PC-based sampling was carried out simultaneously over four channels using a National Instruments PCI-6110E A/D converter card. Data sampling and post-processing were performed with software developed in LABVIEW on 2×10^7 samples of complete acquired signal from each transducer.

2.5 Blade-Passage Modulation Level. Amplitude demodulation (or envelope analysis) is a method of signal analysis, which includes elements of signal treatment in the time and frequency domain. Shaft rotation in hydraulic machinery is a fundamental motion that influences all other phenomena. Turbine blades encounter a nonuniform and nonsteady flow field at the entrance. The dominant frequency contained in the cavitation signal is the blade-passage frequency (BPF). The cavitation signal is modulated by the blade-passage frequency. In order to demodulate signal, bandpass filters are used to extract the other frequencies. The filtered signal is then processed by the Hilbert transform or by full wave rectification to obtain the envelope signal. The Fourier transform of the envelope represents the demodulated spectrum $G_M(f)$. The modulated intensity (power) I_M is then

$$I_M = \int_{f_1}^{f_2} G_M(f)df \qquad (1)$$

Abbot et al. [3] showed that the blade-passage modulation level (BPML) can be used as a measure of cavitation intensity on the blade
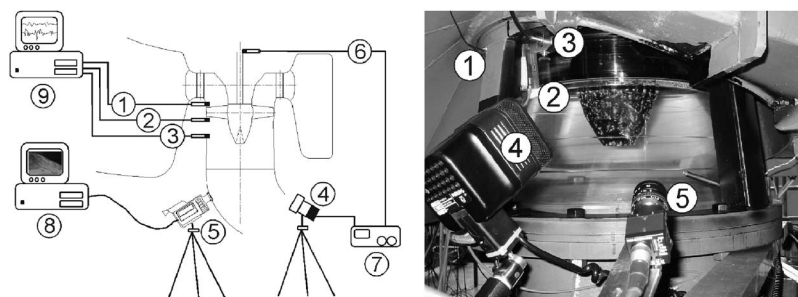
Fig. 2 Experimental setup: 1, accelerometer; 2, hydrophone; 3, AE sensor; 4, stroboscopic light; 5, CCD camera; 6, trigger; 7, stroboscopic main unit; 8, PC with video grabber card; and 9, PC with data acquisition
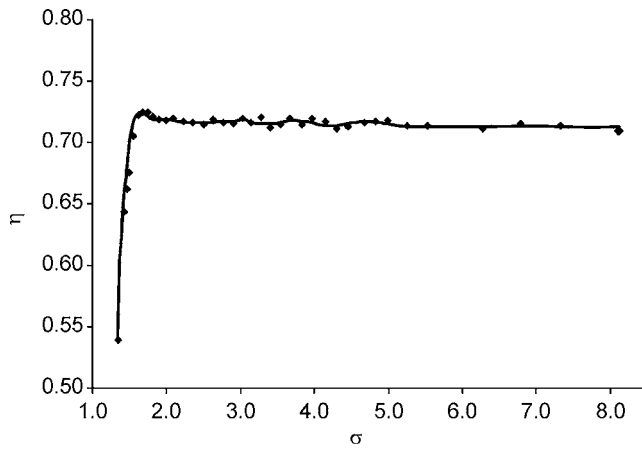
Fig. 3 Two-bladed impeller model efficiency at various cavitation numbers

Fig. 4 Results of measurements with acoustical emission sensor

$$BPML = \sum_{i=1}^{n} G_M(f_i) \qquad (2)$$

where BPML is a sum over blade-passage frequency harmonic lines f_i given in the demodulated spectrum.

The method can disclose the presence of amplitude modulation of the high-frequency noise in hydraulic machinery. Since it is sometimes difficult to distinguish between the basic flow noise (structural and noncavitating) and the cavitation noise, it is useful to apply the same technique also to signals of the noncavitating flow [9].

2.6 Model Turbine Operation Conditions. The present study concentrates on the most severe cavitation conditions, i.e., at the operating point with a full turbine discharge and a minimum full-size turbine operating head. Cavitation measurements were performed at a fixed model turbine head (5.4 m), flow rate (0.44 m^3/s), and rotational speed (900 rpm). Only the cavitation number was changed by adjusting the absolute pressure in the turbine draft tube. The definition of the cavitation number as used in water turbine testing is

$$\sigma = \frac{H_b - H_s - H_v}{H} \qquad (3)$$

where H_b is the atmospheric pressure, H_s is the suction head, H_v gives the vapor pressure of water, and H is the net head applied to the turbine.

At first, a negative suction head was achieved by applying overpressure in the draft tube (measuring points with cavitation number σ higher than 4.6 in Fig. 3), then a vacuum pump was used to achieve positive suction head up to the point of full impeller cavitation. In this way, the full range of cavitation conditions was tested.

3 Results of Measurements

Previous studies showed that signals of acoustical emission, noise, and vibration will rise with decreasing cavitation number, reach a maximum, and then fall in a very low cavitation number region [9]. With the highly cavitating flow, the signal drops because highly compressible two-phase flow attenuates the pressure wave and causes the fall of the measured signal.

In another commonly found trend of the acoustical signal with the cavitation number, one would first observe a rise of the signal to a local maximum, a fall to a local minimum, and a rise again [10,11]. A clear and plausible explanation of such a phenomenon was never given. Present measurements show a similar trend, and this study focuses on explaining this phenomenon.
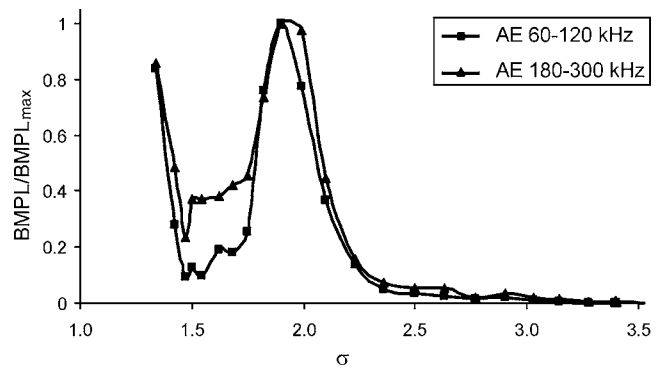
Diagrams of measured signals with three sensors, i.e., the acoustic emission sensor shown in Fig. 4, the hydrophone shown in Fig. 5, and the accelerometer shown in Fig. 6, in different frequency ranges are presented. The data obtained from the acoustic emission sensor, the hydrophone, and the accelerometer are normalized by their maximal values (BPML/BPML$_{max}$).

3.1 Results of Acoustic Emission Measurements. For the acoustical emission measurements (Fig. 4), the frequency range plays no role for the cases with higher cavitation numbers. Both signals (in the frequency ranges of 60–120 kHz and 180–300 kHz) begin to rise at approximately σ=3.4, where cavitation first occurs. A maximum of both signals is reached at σ =1.9. After that, the amplitude of the signals drops significantly until a local minimum is reached at σ=1.5. The amplitude of the signal with the frequency range 180–300 kHz drops slightly slower in this region, probably because the majority of the eigenfrequencies of the pressure waves that are emitted during the cavi-
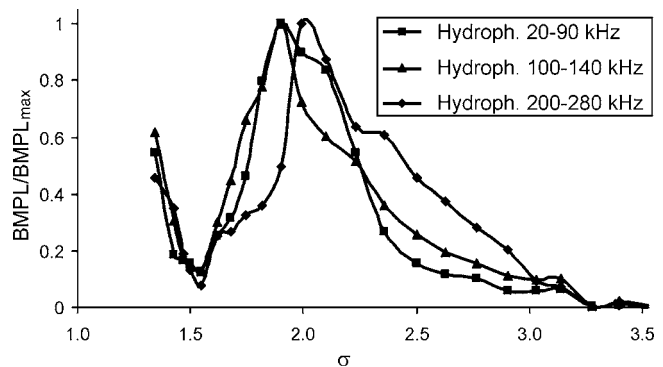

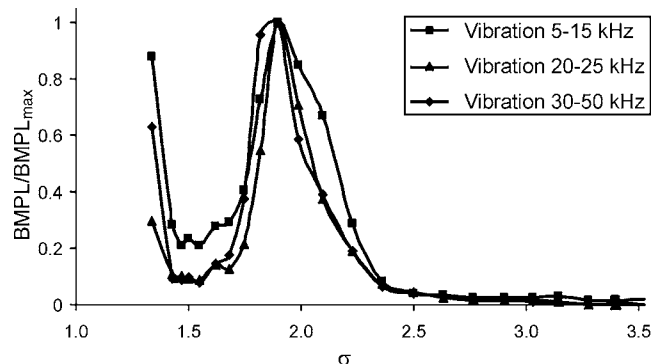Fig. 5 Results of measurements with a hydrophone

Fig. 6 Results of measurements with accelerometer

tation cloud collapse also lie in this range [12,13]. At even lower cavitation numbers ($\sigma < 1.5$), both signals rise again.

3.2 Results of Hydrophone Measurements. For hydrophone measurements (Fig. 5), the frequency range has greater influence on the measured signal amplitude. Similarly to the acoustic emission measurements, the signals begin to rise at incipient cavitation ($\sigma \approx 3.5$). The signal with the frequency from 200 kHz to 280 kHz rises the fastest since it is the closest to the eigenfrequencies of the pressure waves that are emitted during the collapse of vapor structures. The maximum of the three signals is not reached at the same cavitation number—while the signals with the ranges of 20−90 kHz and 100−140 kHz reach it at $\sigma = 1.9$, the signal with the range of 200−280 kHz reaches it at approximately $\sigma = 2.1$. The signal amplitudes drop when the cavitation number is further decreased. Interestingly, the signal with the frequency range of 200−280 kHz drops the fastest. The local minimum is the same for all the frequency ranges at approximately $\sigma = 1.5$. Also, similar signals can be seen in a region with $\sigma < 1.5$.

It seems that the frequency range plays a major role in hydrophone measurements. The sensor responds much quicker (at lower signal magnitude) when the range of frequencies is closer to the eigenfrequency of the measured pressure waves.

It is possible that the structural response of the turbine and other components might affect the measurements, but we believe these effects are negligible in comparison to the signal of cavitation. This is concluded from a noise measurement of nearly as low as 40 dB for a noncavitating condition.

3.3 Results of Vibration Measurements. Accelerometer measurements (Fig. 6) are again less dependent on the range of frequencies. No significant influence can be seen even in the range of 30−50 kHz, where the sensor resonant frequency could have an effect. The signals begin to rise after the incipient cavitation occurs ($\sigma \approx 3.4$). The maximum of all signals is reached at $\sigma \approx 1.9$, and the local minimum occurs at $\sigma = 1.5$. The signals rise when the cavitation number is further reduced ($\sigma < 1.5$).

It is clear that a sufficient explanation of signal trends cannot be given at this stage. The local minima probably correspond to the increased compressibility of the developed cavitating flow. Visualization of cavitation was employed to determine the reason for the increase of the amplitude at very low cavitation numbers.

4 Visualization of Cavitation Structures

A Sony HC-HR50 progressive scan monochrome CCD camera (internal/external synchronization for capturing up to 60 noninterlaced frames per second at maximum resolution of 659×494 pixels) with Pentax C-mount lenses 12 mm f/1.2 and a stroboscopic light were used for image capturing and illumination, respectively. The stroboscopic light and the camera were triggered at a specific rotation angle of the turbine shaft using an inductive sensor. Images of the suction side of one blade were taken simultaneously with the acoustic measurements. For each operating point, 600 images of the same turbine blade were taken during 40 s of data acquisition (turbine revolution speed was 900 rpm). Images were digitalized in real time with a National Instruments PCI-1409 image acquisition board in an eight-bit color depth (256 levels of gray level). In further analysis, only 500 images were retained (100 images with the most differences from the average were further discarded).

Figure 7 shows a typical image for the blade cavitation. One can see the suction side of the blade. The cavitating flow can occur at three typical positions:

- near the impeller hub-hub cavitation
- on the suction side of the blade-blade cavitation
- on the tip of the blade-tip cavitation

It is not necessary for the cavitation to be present at all three positions. The blade cavitation, for example, occurs much later (at
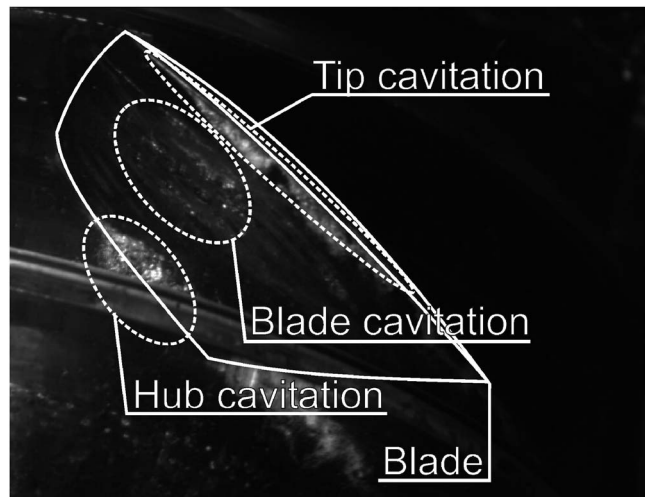

Fig. 7 A typical image with noted places of cavitation occurrence on the blade

a lower cavitation number) than the hub and tip cavitation. The arc that can be seen in the bottom part of the image is the edge of the suction tube (the same applies for the images in Figs. 8–10).

Figure 8 shows typical images of cavitation on the blade at different cavitation numbers. The first operating point at cavitation number $\sigma = 8.11$ displays one-phase liquid flow. Cavitation first appears at cavitation number $\sigma = 3.4$ ($\sigma_{incipient} = 3.4$). At first, cavitation on the hub and on the tip of the blade is present (Fig. 8). The cavitation pockets are first attached to the solid body (to the blade and the hub). The separation of the cavitation clouds occurs
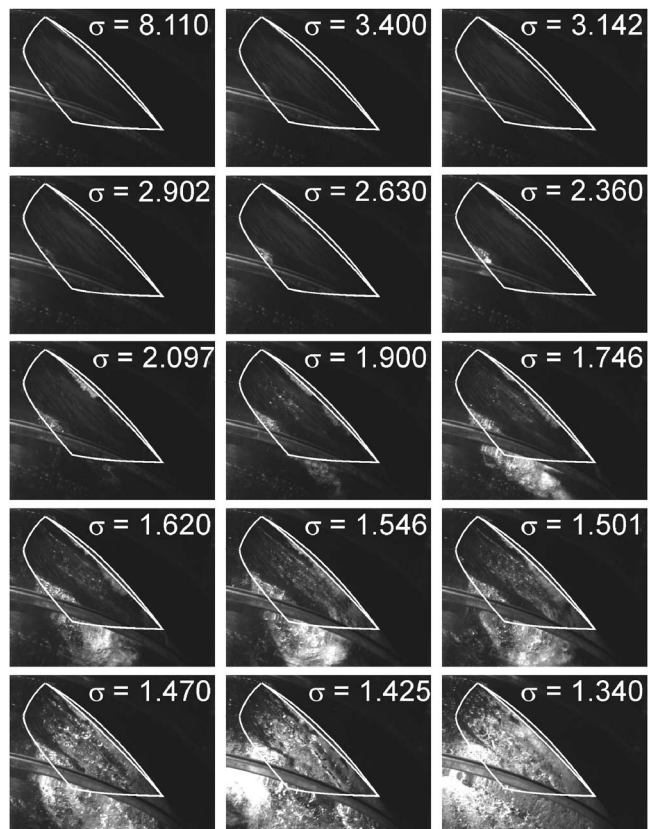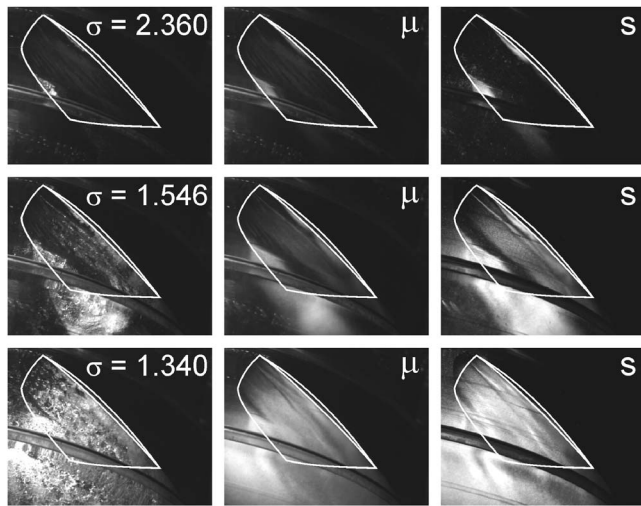

Fig. 8 Typical images of vapor structures at different cavitation numbers

Fig. 9 Image from the series (left), mean value of gray level μ (middle), and standard deviation of gray level s (right) for three cavitation numbers

when the pressure is further decreased—at approximately $\sigma = 2.63$. The position and type of the cavitation remain unchanged until the cavitation number $\sigma = 2.097$ is reached. At this stage, the hub cavitation changes its type from cloud to bubble cavitation—macroscopic bubbles (radii > 1 mm) appear. Meanwhile, the tip cavitation remains cloudy.

With the decreasing pressure, the cavitation on the hub and the tip grows. At cavitation number $\sigma = 1.9$, the cavitation on the surface of the blade appears in the form of macroscopic bubbles (bubble cavitation). The types of cavitation remain the same (hub bubble cavitation, blade bubble cavitation, and tip cloud cavitation) until the pressure is decreased to the limit where supercavitation on the blade occurs. The first glimpse of supercavitation can be seen at cavitation number $\sigma = 1.425$; the cavitation covers en-
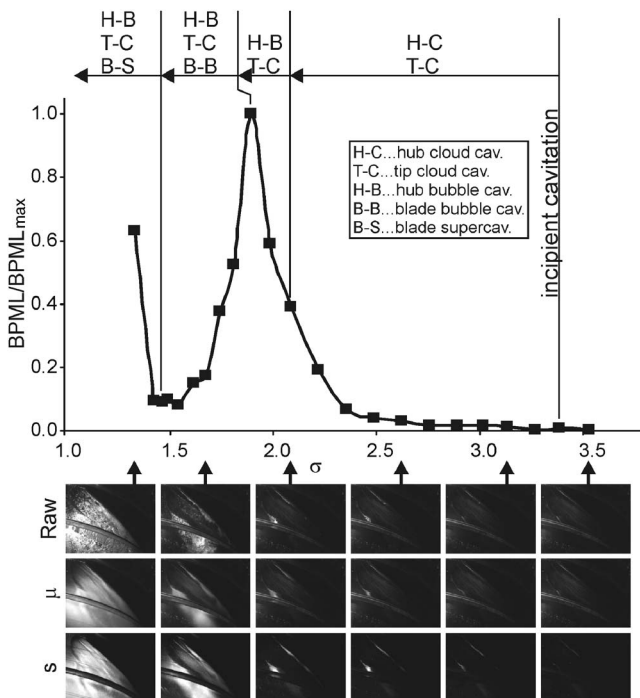
Fig. 10 A typical diagram of acoustical measurements with noted corresponding cavitation types and positions

tirely the blade at cavitation number 1.34. Meanwhile, it seems that the tip cavitation remains cloudy and the cavitation on the hub remains bubbly.

4.1 Image Post-Processing. Image post-processing is based on the fact that image n with ij pixels can be presented as a matrix with ij elements. With eight-bit resolution, there are 256 levels of gray level for $A(i,j,n)$, in which the matrix element can be 0 for black pixel and 255 for white pixel

$$A(i,j,n) \in \{0, 1, \dots 255\} \tag{4}$$

Each image is presented as a matrix

$$\text{Image}(n) = \begin{pmatrix} A(1,1,n) & \cdots & A(i,1,n) \\ A(1,2,n) & \cdots & A(i,2,n) \\ \vdots & \ddots & \vdots \\ A(1,j,n) & \cdots & A(i,j,n) \end{pmatrix} \tag{5}$$

Interesting parameters are the mean value of gray level, $\mu(i,j)$, and the standard deviation of gray level, $s(i,j)$, of the ijth matrix element in the series of N images

$$\mu(i,j) = \frac{1}{N} \sum_{n=1}^{N} A(i,j,n) \tag{6}$$

$$s(i,j) = \sqrt{\frac{1}{N-1} \sum_{n=1}^{N} [A(i,j,n) - \mu(i,j)]^2} \tag{7}$$

Results of functions $\mu(i,j)$ and $s(i,j)$ are best presented as contour diagrams in matrix form,

$$\mu(i,j) = \begin{pmatrix} \mu(1,1) & \cdots & \mu(i,1) \\ \mu(1,2) & \cdots & \mu(i,2) \\ \vdots & \ddots & \vdots \\ \mu(1,j) & \cdots & \mu(i,j) \end{pmatrix} \tag{8}$$

$$s(i,j) = \begin{pmatrix} s(1,1) & \cdots & s(i,1) \\ s(1,2) & \cdots & s(i,2) \\ \vdots & \ddots & \vdots \\ s(1,j) & \cdots & s(i,j) \end{pmatrix} \tag{9}$$

Convergence of the mean value and the standard deviation of gray level was studied to determine the minimum number of images that need to be included in the post-processing. The uncertainty level of <1% for the mean value and <1.5% for the standard deviation was estimated for the case with 50 images [8].

4.2 Results of Image Post-Processing. In all, 500 images for each operating point were used for the statistical evaluation of cavitation. The mean value and standard deviation of gray level of images were calculated. Figure 9 shows results of statistical evaluation of images for three characteristic cavitation numbers ($\sigma = 2.36$, 1.546, and 1.340). The left image in Fig. 9 is from each series, the middle image represents the mean value of gray level μ, and the right one represents the standard deviation of gray level s. We can interpret the mean value of the gray level as a parameter that is related to the mean vapor volume fraction. Similarly, one can look at the standard deviation of the gray level as a parameter that defines the activity (dynamics) of cavitation. We can conclude that both the vapor volume fraction and the dynamics of cavitation increase as the cavitation number is reduced.

It is known that the cavitation appearance becomes stable as the state of supercavitation is reached. In contrast to this, the standard deviation increases. This is probably because the steady free surface between the liquid and the vapor phase is still slightly oscillating, but not in a form of cavitation cloud separations. This phenomenon was more thoroughly investigated by Dular et al. [8].

Besides an expected increase of cavitation aggressiveness, the

damping effects, which can be related to the vapor volume fraction [14], will also increase. In the following sections, a discussion of the effect of the increase in attenuation as a possible reason for the measured signal trend is presented.

5 Discussion

Since the signals of acoustical measurements (Figs. 4–6) do not vary significantly, the explanation and discussion of the relationships between the acoustical measurements and cavitation appearance are, in essence, the same for all the measured signals. Hence, only the relation between the hydrophone measurements in the range of 100–140 kHz and cavitation images is thoroughly discussed. The conclusions stated in this section are also valid for other measurements (vibration, acoustic emission, and other hydrophone measurements).

Figure 10 shows the measured evolution of the hydrophone signal (100–140 kHz) and the corresponding cavitation types and positions. Inset pictures show raw images, mean values, and standard deviations at specific operating points.

The signal starts to rise after the incipient cavitation occurs (at $\sigma = 3.4$). As mentioned before, first the cavitation on the hub of the impeller and on the tip of the blade occur. Both regions of cavitation are cloudy (the bubble sizes are up to 20 μm) and attached. The signal rises exponentially as the cavity grows, and the cloud separations begin to occur. At approximately $\sigma = 2.1$, the cloud cavitation on the hub becomes partially bubbly—macroscopic bubbles appear, the diameter of which are on the order of a few millimeters. It is known that an implosion of a single macroscopic bubble is usually less aggressive than an implosion of a cloud of microscopic bubbles [13]. This is probably the reason that a small decrease in the gradient of the amplitude versus σ can be seen in the diagram at this point (Fig. 10, and also in other diagrams of acoustical measurements, Figs. 4–6). The gradient increases again, after the tip cavitation grows slightly (at $\sigma \approx 2$). At cavitation number $\sigma = 1.9$, a maximum of the acoustical signal is reached. At this stage, the blade starts to cavitate in the form of macroscopic bubbles. If we move to the next operating point ($\sigma = 1.746$), then the acoustical signal falls dramatically. The cavitation on the other hand grows. The reason probably lies in the fact that the hub cavitation grows to the point when it "chokes" itself—the pressure wave that is emitted at a cloud collapse is attenuated in a highly compressible two-phase bubbly flow region. The pressure wave amplitude that comes from the hub cavitation is, in fact, smaller at $\sigma = 1.746$ than at $\sigma = 1.9$, where the cavitation extent is smaller. The gradient of the acoustical curve decreases when the cavitation number is decreased. This is because the extent of the cavitation increases—while the part of the detected signal from the hub cavitation decreases, parts of the signal from the tip and the blade cavitation increase. They are not influenced by the attenuation of the two-phase bubbly flow. The local minimum is reached at approximately $\sigma = 1.5$. When the cavitation number is further reduced, the cavitation pocket covers the whole blade—supercavitation occurs. Here (at $\sigma < 1.5$), a free surface between the liquid and vapor phase exists. This situation is unique, since the compressibility of individual phases is much smaller than that of the bubbly two-phase flow, which was present at higher cavitation numbers. The emitted pressure waves are again faced with a smaller attenuation; hence, the detected amplitudes are higher at very small cavitation numbers.

6 Model Development

On the basis of the above-mentioned interpretations, we can formulate a physical model that links the information gained by the visualization of cavitation structures to the results of measurements of cavitation noise and vibration. This model is very similar to the cavitation erosion model developed by Dular et al. [15,16] that uses data from visualization as input for the prediction of the
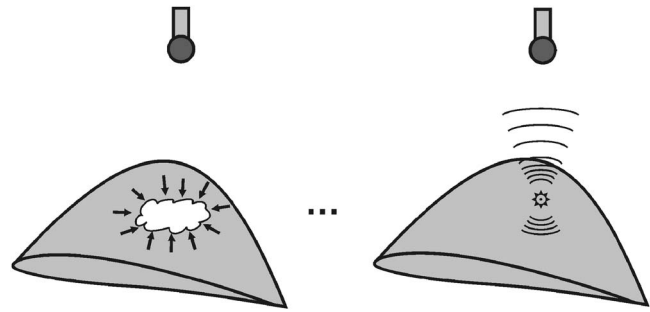

Fig. 11 Principle on which the model is based

distribution and the magnitude of damage. This can be done because the processes of cavitation erosion and cavitation noise and vibration are strongly linked [19].

The phenomenon of cavitation noise generation is complex and can be looked on as a sequence of several processes. The presented theory explains it in the following way (Fig. 11):

- Collapse of the cavitation cloud causes a shock wave that spreads in the fluid.
- The magnitude of the shock wave is attenuated as it travels through the fluid.
- The attenuation of the shock wave is predominately a function of the vapor volume fraction of the region through which it travels.

Although results of acoustic measurements imply otherwise, the cavitation aggressiveness (which would be manifested in effects such as cavitation erosion) probably gradually increases as the cavitation number is decreased and does not follow the trend measured by acoustical sensors, which are positioned "far" away [8,19]. This hypothesis was partially confirmed by erosion tests from previous studies on similar geometries, where increase in erosion was found when the cavitation number was lowered [20,21]. The measured trend is very probably solely a result of attenuation of the pressure wave by the region between the cavitation and the sensor.

6.1 Amplitude of the Emitted Pressure Wave. The power and, consequently, the magnitude of the emitted pressure wave are closely related to the velocity of the change of the vapor cloud volume (velocity of cavitation cloud collapse) and to the surrounding pressure [22]. We can write the following relation:

$$P_{\text{wave}} = \Delta p \left(\frac{dV}{dt} \right) \qquad (10)$$

where Δp is the difference between the surrounding pressure and vapor pressure ($p_{\text{sur}} - p_v$) and dV/dt is the change of the vapor cloud volume in time t.

The magnitude of the emitted pressure wave is proportional to the square root of its power ($p_0 \propto \sqrt{P_{\text{wave}}}$). If we consider the surrounding pressure to remain approximately constant, then we can write that the distribution of the mean change in cavitation cloud volume reveals the mean distribution of amplitude of the pressure wave that is emitted by the cavitation cloud collapse.

Since the measurements of the instantaneous change of the cavitation cloud volume is not possible (the image-capturing frequency was much lower than the frequency of vapor cloud shedding), a standard deviation of gray level was used as the parameter to be related to the power of the emitted pressure wave. Standard deviation can be used in this manner since it is a function of the change of the gray level in the image as well as the cavitation cloud volume. This hypothesis was confirmed by comparing results of the standard deviation and the time derivative of a sequence of images using high-speed movie [23].

Journal of Fluids Engineering

$$\text{gray level} = f(V) \Rightarrow s \propto \left(\frac{dV}{dt}\right) \tag{11}$$

The hypothesis is that the relation between the time derivative of vapor cloud volume and the distributions of standard deviation of gray level exists. A measure of the emitted pressure wave power P_{wave} can be simply formulated in the following way:

$$P_{\text{wave}} \propto \Delta p \sum_i \sum_j s_{ij} \tag{12}$$

where Δp is the mean pressure difference and s is the standard deviation of a pixel in the series of images. It was found by comparison of model predictions and from results of experimental measurements of the emitted pressure wave magnitude by Hofmann [24] that a linear function shows the best correlation to the experimental results [15,16],

$$p_0 = k\sqrt{P_{\text{wave}}} = k\sqrt{\Delta p \sum_i \sum_j s_{ij}} = k_1 \frac{\sqrt{\Delta p \sum_i \sum_j s_{ij}}}{\left[\sqrt{\Delta p \sum_i \sum_j s_{ij}}\right]_{\text{max}}} \tag{13}$$

In order to simplify the calculation at each operating point, the expression inside the square root was normalized by its maximal value (in this case, it occurred at the cavitation number $\sigma = 1.34$).

6.2 Attenuation of the Pressure Wave. As the pressure wave travels away from its source, its energy is gradually converted into heat. For our problem, the main energy loss mechanism is the viscous losses generated from the friction within the fluid itself [14]. In the present case, the pressure wave passes a highly compressible two-phase region and also a single (liquid) phase region before it arrives at the sensor (except for the last three operating points, where supercavitation is present and only two regions with small compressibility exist). The wave magnitude is attenuated with distance x from the source according to

$$p = p_0 e^{-(2/3)(\omega^2/\rho c^3)\eta x} \tag{14}$$

where ω is the pressure wave frequency, η and ρ are the viscosity and the density of the fluid through which the pressure wave travels, respectively, and c is the sonic velocity within the fluid through which the pressure wave travels. The quantities ρ, η, and c, are functions of the local vapor volume fraction α. The vapor volume fraction α of the region where the pressure wave travels through (the region between the cavitation cloud and the sensor) can be related to the mean value of the gray level of the cavitation images [25]. For the present study, the following relation was used:

$$\alpha = f(\mu) = k \sum_i \sum_j \mu_{ij} = k_2 \frac{\sum_i \sum_j \mu_{ij}}{\left[\sum_i \sum_j \mu_{ij}\right]_{\text{max}}} \tag{15}$$

A maximal value was used to normalize the function.

6.3 Consideration of Sonic Velocity and Fluid Properties. Experimental results show obvious influences of fluid properties on cavitation aggressiveness. For example, it was shown that when the experiment was conducted in water with high gas content cavitation aggressiveness (the amplitude of acoustical signals) was smaller [8]. The main reason lies in the fact that the sonic velocity is lower in water with high gas content. Consequently, compressibility and pressure wave attenuation are higher. To consider these effects, one has to introduce the properties of two-phase bubbly mixture to the model.

The sonic velocity of fluid with the presence of gas bubbles is given by [12]
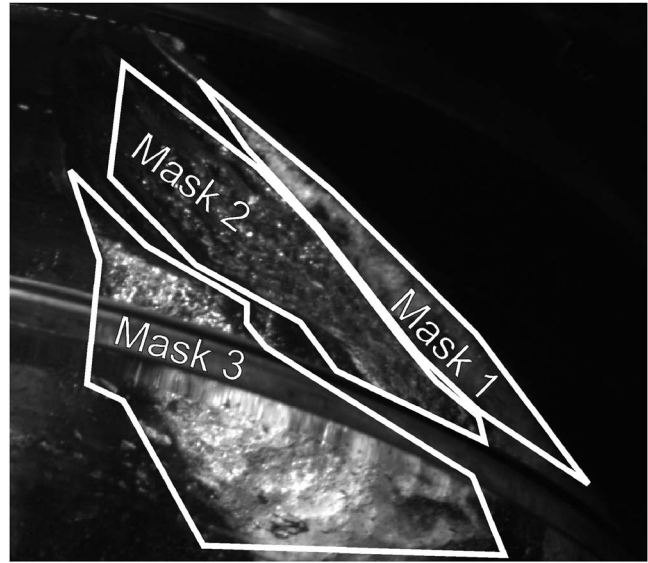
Fig. 12 Positions of masks that define different positions of cavitation occurrence

$$c = \left\{ \left[\rho_l(1-\alpha) + \rho_g \alpha\right] \left(\frac{\alpha}{\kappa p_{\text{sur}}} + \frac{1-\alpha}{\rho_l c_l^2}\right) \right\}^{-(1/2)} \tag{16}$$

where ρ_l and ρ_g are the density of the liquid and gas, respectively, α is the gas volume fraction, and κ the polytropic constant of the gas. The density and viscosity of the fluid considering the presence of gases are

$$\rho = \alpha \rho_g + (1-\alpha)\rho_l \tag{17}$$

and

$$\eta = \alpha \eta_g + (1-\alpha)\eta_l \tag{18}$$

Results of Eqs. (16)–(18) are included in the "final model equation"—Eq. (20), where parameters of the fluid (sonic velocity, density, and viscosity) through which the pressure wave travels are considered.

6.4 Formulation of the Integral Pressure Wave Amplitude. The noise or vibration detected contains signals from cavitation from the hub, blade, and tip. We must consider that pressure wave first travels through a two-phase flow and then also through a single-phase liquid flow before it reaches the sensor. The pressure wave from a specific cavitation location is in respect to attenuation rate (Eq. (14)); therefore,

$$p_{\text{sig}} = \left(p_0 e^{-(2/3)(\omega^2/\rho_{2p} c_{2p}^3)\eta_{2p} x_{2p}}\right) e^{-(2/3)(\omega^2/\rho_l c_l^3)\eta_l x_l} \tag{19}$$

The expression in the parentheses defines the amplitude of the pressure wave on the boundary of the cavitation pocket (variables ρ, η, c, and x correspond to two-phase fluid—index $2p$). The added exponential function defines additional attenuation of the pressure wave amplitude due to friction in single (pure liquid) flow (variables ρ, η, c, and x correspond to pure liquid fluid—index l). Finally, the pressure wave amplitude can be defined as the sum of the pressures from specific locations defined by the mask (Fig. 12) (from hub, blade, and tip)

$$p_\Sigma = \left(p_{0,\text{hub}} e^{-(2/3)(\omega^2/\rho_{2p,\text{hub}} c_{2p,\text{hub}}^3)\eta_{2p,\text{hub}} x_{2p,\text{hub}}}\right) e^{-(2/3)(\omega^2/\rho_l c_l^3)\eta_l x_{l,\text{hub}}}$$
$$+ \left(p_{0,\text{blade}} e^{-(2/3)(\omega^2/\rho_{2p,\text{blade}} c_{2p,\text{blade}}^3)\eta_{2p,\text{blade}} x_{2p,\text{blade}}}\right)$$
$$\times e^{-(2/3)(\omega^2/\rho_l c_l^3)\eta_l x_{l,\text{blade}}}$$
$$+ \left(p_{0,\text{tip}} e^{-(2/3)(\omega^2/\rho_{2p,tip} c_{2p,tip}^3)\eta_{2p,\text{tip}} x_{2p,\text{tip}}}\right) e^{-(2/3)(\omega^2/\rho_l c_l^3)\mu_l x_{l,\text{tip}}} \tag{20}$$

Table 1 Values of parameters used in the model

Region/coefficient	k_1 (Pa)	k_2	k_3 (m)	x_1 (m)
Hub cavitation	6×10^6	0.3	0.07	0.2
Blade cavitation	6×10^6	0.987	0.03	0.1
Tip cavitation	6×10^6	0.241	0.01	0.01

The acoustical path considered in Eq. (20) does not entirely reflect the complicated physical situation with the pressure waves bouncing from different solid surfaces. The simplification is, however, reasonable since the possible reflected pressure wave is for an order of magnitude smaller because of the high frequency and additional viscous attenuation and energy loss at reflection.

6.5 Relation Between the Pressure Wave Amplitude and the Acoustic Pressure. The acoustic pressure is by definition the pressure variation around the mean pressure. We presumed that the acoustic pressure amplitude is proportional to the pressure wave amplitude p_Σ (the acoustic pressure amplitude rises with increasing pressure wave amplitude).

One can make such an assumption, since it is the pressure wave p_Σ that causes cavitation effects (such as erosion) and, therefore, noise generation. The aggressiveness of these effects (and, consequently, the generation of noise) is proportional to the amplitude of the pressure wave p_Σ [19].

6.6 Acquiring the Data From the Images. As we can see (Eqs. (13) and (15)), we need to acquire the data composed of the mean values and the standard deviations of the gray level to determine the parameters of vapor volume fraction and the intensity of cavitation implosion at the specific region (hub, blade, and tip). For this purpose, masks were used so that only the gray level from the desired region was considered for post processing (Fig. 12).

Another problem occurs when the shock wave travels through the cavitation cloud. The thickness of the cavitation cloud defined as $x_{2p,\text{hub}}$, $x_{2p,\text{blade}}$, and $x_{2p,\text{tip}}$ in Eq. (20) are approximated as the functions of the mean value of the gray level in the region and expressed as

$$x_{2p} = k \sum_i \sum_j \mu_{ij} = k_3 \frac{\sum_i \sum_j \mu_{ij}}{\left[\sum_i \sum_j \mu_{ij} \right]_{\max}} \qquad (21)$$

Again normalized values were used. Values of coefficients k_1, k_2, k_3, and the distances between the cavitation at the specific region and the sensor $x_{l,\text{hub}}$, $x_{l,\text{blade}}$, and $x_{l,\text{tip}}$ are given in Table 1.

To determine the values of coefficients k_1, k_2, and k_3 that are used in Eqs. (13), (15), and (21) information from literature and some iterations are required. The shock wave magnitude at its origin has not yet been experimentally determined because of the effect of attenuation, but theoretical work by Brennen [12] and Shimada et al. [13] set it on the order of 6 MPa. Some help was also gained from experimental measurements of the shock waves on similar geometries from Hofmann [24]. It was also shown by the present authors [8] that using the value of 6 MPa works well for prediction of the pressure wave amplitude. The coefficient k_1 was chosen to fulfill the physical and empirical (from past studies [12,13,24]) considerations of the shock wave values, so the maximum pressure wave amplitude of 6 MPa was assumed ($k_1 = 6$ MPa).

The coefficient k_2 varies significantly from one region to another, since the vapor volume fraction varies according to the type of cavitation (Fig. 8). The values were derived by iteration, but physical background was considered. It can be seen from the single images (Fig. 8) that, for the case of hub and tip cavitation, maximal volume fraction does not reach values near to unity. This
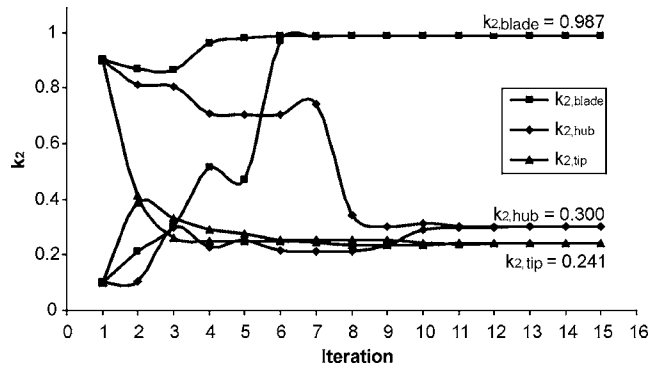
Fig. 13 Evolution of values of parameter k_2 during iterations

is because the vapor volume fraction is relatively low in cloud and bubble cavitation. For example, Stutz and Reboud [26] report on measurements of void fractions, where maximal values of up to $\alpha = 0.4$ for the case of cloud cavitation were found. Hence, a maximum value of vapor volume fraction (coefficient k_2) of $\alpha = 0.4$ ($k_{2,\max} = 0.4$) for these two regions was expected and also found. On the other hand, in the region of blade cavitation, almost a single vapor phase was approximated, since a supercavitation region exists here in the case of a maximum (Fig. 8). The final values of coefficient k_2 were then determined by iteration until the best correlation between the experiment and the model prediction was found. The values are in agreement with experimental data from past measurements of vapor volume fraction in cavitating flow [26]. The evolution of values of k_2 for each iteration step are presented in Fig. 13. One can see that the values $k_{2,\text{hub}}$, $k_{2,\text{blade}}$, and $k_{2,\text{tip}}$ converge to the final values regardless of the initial value (cases for initial values of 0.1 and 0.9 are presented). The coefficient k_3 defines the maximal thickness of cavitation—values were measured directly from the images. The values of densities and viscosities of water and water vapor (ρ_l, ρ_v, ν_l, ν_v) and the sonic velocity (c_l) and water vapor pressure (p_v) correspond to the ambient temperature of 20°C. The system (surrounding) pressure was $p_{\text{sur}} = 22,500$ Pa.

A value of $f = 0.5$ MHz for frequency of the pressure wave was chosen on the basis of studies of Shimada et al. [13] and Lohrberg et al. [19] and also on the basis of measurements of pressure waves on similar geometries done by Hofmann [24].

In order to present the model in a clearer way, Fig. 14 shows the whole path from image capturing to the prediction of the pressure wave amplitude for one operating point (one cavitation number):

1. 500 images of cavitation structures are captured (Fig. 8).
2. By means of statistical evaluation (Eqs. (5)–(9)), the mean value and the standard deviation of the images are determined (Fig. 9).
3. Masks that determine the position of cavitation are generated (Fig. 12).
4. Parameters in Table 1 (k_1, k_2, k_3, and x_l) are determined on the basis of references, iteration and present experiment (see Sec. 6.6).
5. p_0 ($p_{0,\text{hub}}$, $p_{0,\text{blade}}$, $p_{0,\text{tip}}$) is calculated by Eq. (13), where matrix of standard deviation is used as an input. Masks and parameters from Table 1 are also used in this step.
6. Void fractions α for each region (hub, blade, and tip) are calculated by Eq. (15), where matrix of mean value is used as an input. Masks and parameters from Table 1 are also used in this step.
7. Physical properties and void fractions α are used to determine the properties of the two-phase flow region through which the acoustic wave travels ($\eta_{2p,\text{hub}}$, $\eta_{2p,\text{blade}}$, $\eta_{2p,\text{tip}}$, $\rho_{2p,\text{hub}}$, $\rho_{2p,\text{blade}}$, $\rho_{2p,\text{tip}}$, $c_{2p,\text{hub}}$, $c_{2p,\text{blade}}$, $c_{2p,\text{tip}}$) (Eqs. (16)–(18)).
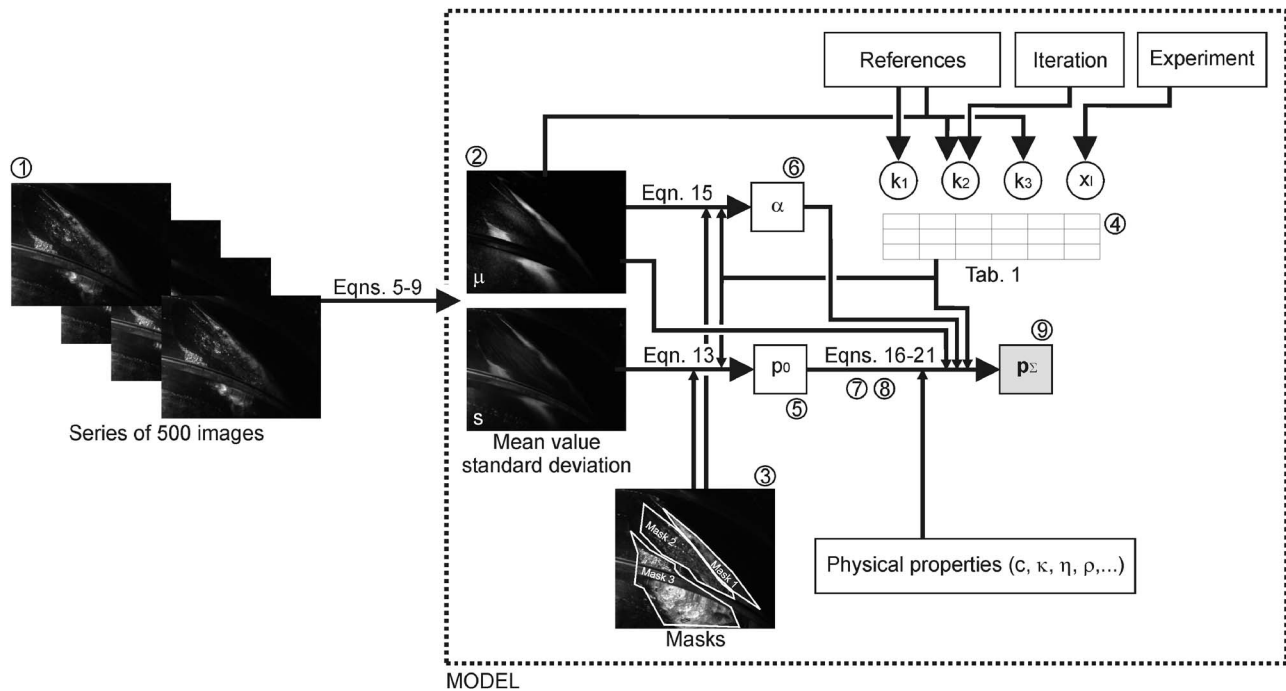
Fig. 14 Graphical representation of the model structure

8. The thickness of the cavity ($x_{2p,\text{hub}}$, $x_{2p,\text{blade}}$, $x_{2p,\text{tip}}$) is calculated by Eq. (21), where parameters from Table 1 are used as an input.

9. By introducing parameters of single (pure liquid) fluid (η_l, ρ_l, c_l) and distances between the cavity and the sensors ($x_{l,\text{hub}}$, $x_{l,\text{blade}}$, $x_{l,\text{tip}}$), attenuation rate and, finally, the sum of the pressure wave amplitude are calculated by Eq. (20).

7 Results of Predictions

As already mentioned, we made a presumption that the acoustic pressure amplitude is proportional to the pressure wave amplitude p_Σ and that the acoustic pressure amplitude rises with increasing pressure wave amplitude. Hence, a comparison of results of measurements of acoustic emission in the frequency range from 60 kHz to 120 kHz and the model prediction of the pressure wave amplitude is shown in Fig. 15.

One can obviously see the resemblance of the two curves. The model predicts that the pressure wave amplitude begins to rise as cavitation first appears (at cavitation number $\sigma = 3.4$). The predicted pressure wave amplitude exponentially rises as the cavita-
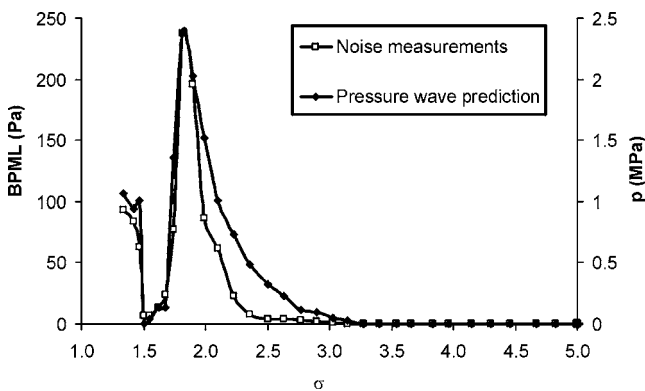
tion number is decreased and reaches a maximum at the same operating condition at which the maximum of acoustic emission was measured (at cavitation number $\sigma = 1.9$). The model then correctly predicts the decrease in pressure wave amplitude and later an increase as the operating pressure (cavitation number) is lowered. The maximal predicted amplitude of the pressure wave is ~ 2.4 MPa, which corresponds very well to the measurements of Hoffman [24].

For better understanding of how the model works, it is convenient to plot the individual contributions of each cavitation region (hub, tip, and blade), which adds to the sum of the pressure wave amplitude (Fig. 16). The model predicts that the pressure wave from the tip cavitation will rise exponentially as the cavitation number decreases. It will reach a maximum at approximately $\sigma = 1.9$. Then a sudden decrease occurs as a result of "choking." Its predicted amplitude falls to almost 0 at $\sigma = 1.5$. After that, supercavitation occurs and a signal of higher amplitude is predicted. As can be expected, the cavitation on the tip of the blade adds the
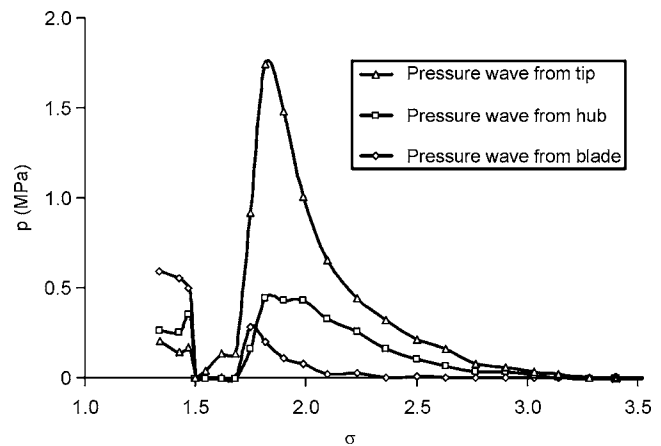

Fig. 15 Results of noise measurements and model predictions of the pressure wave amplitude

Fig. 16 Predicted pressure wave contributions of each cavitation region

biggest portion to the sum of the predicted pressure wave amplitude. This is because it is the closest to the sensors' location, and therefore, the attenuation is the smallest.

In the case of hub cavitation, the model predicts a monotone increase of cavitation intensity until a plateau is reached at σ = 2.0. The predicted pressure wave from this region stays almost constant until σ = 1.8 is reached and then falls to a negligible value. Similarly to the case of tip cavitation, a pressure wave is predicted as the cavitation in this region takes the form of super-cavitation.

In contrast to hub and tip cavitation, the blade cavitation occurs later (at a lower cavitation number). Its influence is first predicted at σ = 2.3, but the pressure wave amplitude does not increase significantly until σ = 1.8. After that, the intensity decreases to almost 0. Again at σ = 1.5 in the regime of supercavitation, an increase of the pressure wave amplitude was predicted.

8 Conclusions

A study of acoustical measurements on a two-bladed Kaplan turbine model in various cavitating conditions was presented. Interesting results that could not be unveiled previously were obtained. As the cavitation number was decreased, all signals experienced a maximum, local minimum, and later (at even lower cavitation numbers) another increase in amplitude. Visualization of the cavitation was done, and a relatively simple statistical evaluation of captured images was performed. A hypothesis that the mean value of the gray level is related to the local vapor volume fraction and that the standard deviation of the gray level is related to the dynamics of cavitation was made on the basis of previous studies.

The inspection of single images revealed that different cavitation types exist at various positions on the turbine blade as a function of cavitation number. This fact indicates a possible explanation of the variation of acoustic emission, noise, and vibration based on the topological structure and the position of cavitation.

It is hypothesized that the attenuation of the pressure wave causes the distinctive signal trend and the cavitation aggressiveness increases while the cavitation number is lowered. This was done on the basis of previous experiments [20,21]. A corresponding semi-empirical model was developed, and its prediction result agrees very well with the measured signals.

Nomenclature

A = gray level value of pixel
BPML = blade-passage modulation level (Pa)
BPML_{max} = maximal blade-passage modulation level (Pa)
c = sonic velocity (m/s)
c_l = liquid sonic velocity (m/s)
f = frequency (Hz)
G_M = demodulated spectrum
H = net head (m)
H_b = barometric head (m)
H_s = suction head (m)
H_v = vapor head (m)
i = pixel coordinate
I_M = modulated intensity
j = pixel coordinate
k_1 = empirical coefficient (Pa)
k_2 = empirical coefficient
k_3 = empirical coefficient (m)
l = blade chord length (m)
n = image number
n_q = turbine specific speed $n_q = \omega \sqrt{Q} / \sqrt[4]{(gH)^3}$
N = number of images
p = pressure wave amplitude (Pa)
p_{sig} = pressure wave amplitude from a specific location (Pa)
p_{sur} = surrounding pressure (Pa)
p_v = vapor pressure (Pa)
p_Σ = integral pressure wave amplitude (Pa)
Δp = pressure difference (Pa)
p_0 = pressure wave amplitude at its source (Pa)
P_{wave} = pressure wave power (W)
Q = volume flow (m^3/s)
Re = Reynolds number Re=ul/ν
s = standard deviation
t = time (s)
V = volume (m^3)
u = blade tip velocity (m/s)
x = distance (m)
x_1 = distance in liquid (m)
x_{2p} = distance in two-phase flow (m)
α = vapor volume fraction
η = dynamic viscosity or efficiency (Pa s)
η_l = liquid dynamic viscosity (Pa s)
η_v = vapor dynamic viscosity (Pa s)
κ = polytropic constant
μ = mean value
ν = kinematic viscosity (m^2/s)
ρ = density (kg/m^3)
ρ_l = liquid density (kg/m^3)
ρ_v = vapor density (kg/m^3)
σ = cavitation number (Eq. (1))
ω = pressure wave frequency and revolution speed (rad/s)

References

[1] Castellini, P., and Santolini, C., 1998, "Vibration Measurements on Blades of a Naval Propeller Rotating in Water With Tracking Laser Vibrometer," Measurement, **24**(1), pp. 43–54.
[2] Bajic, B., 1996, "Vibroacustical Diagnosis of Hydroturbine Cavitation: Some Measurement and Analysis Methods, Modelling," Testing & Monitoring for Hydro Powerplants Conference Papers, Lausanne, pp. 169–178.
[3] Abbot, A., Gedney, C. J., and Greeley, S. D., 1986, "Cavitation Monitoring of Two Axial-Flow Hydroturbines Using Novel Acoustic and Vibration Methods," *13th IAHR Symposium Proceedings*, vol. 1, Paper 23, Montreal.
[4] Neill, G. D., Reuben, R. L., and Sandford, P. M., 1997, "Detection of Incipient Cavitation in Pumps Using Acoustic Emission," Proc. Inst. Mech. Eng., Part E: J. Process Mech. Eng., **211**(4), pp. 267–277.
[5] Alfayez, L., Mba, D., and Dyson, G., 2005, "The Application of Acoustic Emission for Detecting Incipient Cavitation and the Best Efficiency Point of a 60 kW Centrifugal Pump: Case Study," NDT & E Int., **38**(5), pp. 354–358.
[6] Kaye, M., Holenstein, A., Dupont, P., and Rettich, J., 1996, "Acoustic Methods for Monitoring Mechanical Seal Condition and Cavitation Erosion in Hydro Machinery," Modelling, Testing & Monitoring for Hydro Powerplants Conference Papers, Lausanne, pp. 179–188.
[7] Pereira, F., Avellan, F., and Dorey, J. M., 1995, "Cavitation Erosion: Statistical Analysis of Transient Cavities," Int. Symp. on Cavitation—Cav'95, Deauville.
[8] Dular, M., Bachert, B., Stoffel, B., and Sirok, B., 2004, "Relationship Between Cavitation Structures and Cavitation Damage," Wear, **257**(11), pp. 1176–1184.
[9] Kern, I., Rus, T., Hocevar, M., Djelic, V., and Sirok, B., 1999, "Study of Topological Structures of Cavitation With Dynamical Analysis and Computer Aided Visualization," 20th IAHR WG1 Meeting, Brno.
[10] Pearsall, I. S., 1966, "Acoustic Detection of Cavitation," Proc. Inst. Mech. Eng., 1-A66-67, **181**, Part 3A, Paper No. 14.
[11] Gopalakrishan, S., 1985, "Modern Cavitation Criteria for Centrifugal Pumps," 2nd International Pump Symposium, College Station.
[12] Brennen, C. E., 1995, *Cavitation and Bubble Dynamics*, Oxford University Press, New York.
[13] Shimada, M., Kobayashi, T., and Matsumoto, Y., 1999, "Dynamics of Cloud Cavitation and Cavitation Erosion," *Proc. of ASME/JSME Fluids Engineering Division Summer Meeting*, San Francisco, CA, FEDSM99-6775.
[14] Beranek, L. L., 1996, *Acoustics*, Acoustical Society of America, New York.
[15] Dular, M., Stoffel, B., and Širok, B., 2005, "Method for Cavitation Erosion Prediction—Model Development," ASME Fluids Engineering Division Summer Meeting, Houston.
[16] Dular, M., Stoffel, B., and Širok, B., 2006, "Development of a Cavitation Erosion Model," Wear, **261**(5/6), pp. 642–655.
[17] IEC, 1999, *International Standard IEC 60193: Hydraulic Turbines, Storage Pumps and Pump-Turbines—Model Acceptance Tests*, 2nd ed. The International Electrotechnical Commission, Geneva, Switzerland.
[18] ANSI, 2002, *ASTM E650-97: Standard Guide for Mounting Piezoelectric*

Acoustic Emission Sensors, American National Standards Institute, West Conshohocken, PA.

[19] Lohrberg, H., Voss, B., Schlachta, C., Stoffel, B., and Glesner, M., 2002, "Impeller Integrated Measurement of Cavitation Erosive Aggressiveness," Mechatronics, **12**(8), pp. 1047–1057.

[20] Bachert, B., Ludwig, G., Stoffel, B., Širok, B., and Novak, M., 2003, "Experimental Investigations Concerning Erosive Aggressiveness of Cavitation in Radial Test Pump With the Aid of Adhesive Copper Films," 5th International Symposium on Cavitation, Osaka.

[21] Bachert, B., 2004, "Zusammenhang zwischen visueller Erscheinung und erosiver Agressivität kavitierenden Strömungen," Ph.D thesis, Technische Universität, Darmstadt.

[22] Fortes-Patella, R., Reboud, J. L., and Briancon-Marjollet, L., 2004, "A Phe-

nomenological and Numerical Model for Scaling the Flow Aggressiveness in Cavitation Erosion," Workshop on Cavitation Erosion, Bassin d'essais des carenes, Val de Reuil.

[23] Dular, M., 2005 "Development of a Method for the Prediction of Cavitation Erosion in Hydraulic Machines," Ph.D thesis, University of Ljubljana.

[24] Hofmann, M., 2001, "Ein Beitrag zur Verminderung des erosiven Potentials kavitierender Stömungen," Ph.D thesis, Technische Universität Darmstadt.

[25] Wosnik, M., and Arndt, R. E. A., 2006, "Measurements in High Void-Fraction Bubbly Wakes Created by Ventilated Supercavitation," 6th International Symposium on Cavitation, Wageningen.

[26] Stutz, B., and Reboud, J. L., 2000, "Measurements Within Unsteady Cavitation," Exp. Fluids, **29**(6), pp. 545–552.